

Document downloaded from:

<http://hdl.handle.net/10251/183189>

This paper must be cited as:

Medina, M.; Bautista-Rodríguez, A.; Wooldridge, M.; Payri, R. (2021). The effects of injector geometry and operating conditions on spray mass, momentum and development using high-pressure gasoline. *Fuel*. 294:1-10. <https://doi.org/10.1016/j.fuel.2021.120468>



The final publication is available at

<https://doi.org/10.1016/j.fuel.2021.120468>

Copyright Elsevier

Additional Information

The effects of injector geometry and operating conditions on spray mass, momentum and development using high-pressure gasoline

Medina, M., Bautista, A., Wooldridge, M., Payri, R.,

Abstract

High fuel injection pressure (>500 bar) in direct injection gasoline engines is an important means to reduce particulate emissions. While decades of fuel spray research has dramatically advanced the understanding high-pressure diesel fuel sprays, few studies focus on high-pressure gasoline sprays. The objective of this work was to quantify the effects of different injector nozzle geometries on important high-pressure gasoline spray characteristics including injection mass flow rate, momentum flux, and spray imaging at evaporative and non-evaporative conditions. Three categories of nozzle internal geometry were evaluated: inlet rounding; converging-, diverging-, and straight-cylindrical internal flow passages; and different nozzle outlet diameters. Reference grade gasoline was used at injection pressures of 600, 900, 1200, and 1500 bar at chamber pressures from 1 to 30 bar and chamber temperatures from 293 to 800 K. The mass and momentum measurements were used to quantify differences in injector geometry as well as to evaluate for effects of cavitation. The visualization data were analyzed to determine spray penetration and spray angle development for a broad range of operating and state conditions. The results showed internal flow significantly impacts injector performance, where nozzles with inlet rounding resulted in 20% higher mass flow rate compared with straight cylindrical nozzles. Higher fuel injector temperatures also increased mass flow rate by up to 5%. Spray momentum coefficients showed a linear relationship with cavitation number indicating all nozzles were cavitating at all conditions tested. Trends in fuel spray penetration and spray angle development were similar to those observed previously for diesel sprays, which was unexpected given the significant differences in thermal-physical properties of the fuels. Chamber pressure had the strongest influence on penetration distance, and the momentum measurements were good indicators of the injector geometry with the highest penetration distance.

Keywords: High-pressure gasoline, cavitation, schlieren imaging, hydraulic characterization, injector temperature, internal geometry

31 **Introduction**

32 Fuel spray research has advanced dramatically over the past three decades with respect to
33 diesel sprays. Particularly, our understanding of diesel combustion [1], predictions of diesel fuel
34 spray characteristics with semi-empirical correlations [2–4] and effects of operating conditions
35 and injector geometry on diesel fuel spray behavior such as droplet distribution, Sauter Mean
36 Diameter, cavitation, liquid length, cycle-to-cycle variability, apparent heat release, etc. [5–10].
37 Recent advancements in gasoline direct injection (GDI) engines and gasoline compression
38 ignitions (GCI) concepts among other combustion strategies have focused on improving the
39 gasoline fuel injection process [11–13]. However, few previous studies have considered high fuel
40 injection pressures (specifically injections pressures higher than 500 bar) for gasoline, and fewer
41 have considered the early times of the spray development (i.e., transition between momentum
42 and diffusion flow).

43 The previous studies of high-pressure gasoline fuel sprays are briefly summarized here.
44 In the study by Kim et al. [14], the authors compared diesel and gasoline fuel spray development
45 at fuel injection pressures between 400 and 1000 bar at two bar chamber pressure in a constant
46 volume chamber (CVC). The CVC results showed gasoline yielded a shorter liquid penetration
47 length compared with diesel fuel, but the gasoline sprays produced larger spray cone angles. Kim
48 et al. [14] also performed engine studies using an optically-accessible single-cylinder engine and
49 qualitatively compared the spray development of the two fuels at injection pressures of 400 and
50 600 bar. The engine results showed that under evaporating conditions the penetration of gasoline
51 was significantly lower than for diesel. Both fuels yielded comparable peak indicated mean
52 effective pressure, but gasoline combustion resulted in lower NO_x emissions.

53 Unlike the study by Kim et al. [14], the study by Payri et al. [15] showed the penetration
54 distances of diesel and gasoline sprays were similar at fuel injection pressures between 600 and
55 1500 bar in a CVC under non-evaporating conditions. Payri et al. proposed the mixing processes
56 for diesel and gasoline at non-evaporative conditions were the same based on the similar
57 penetration distance and momentum flux measurements for both fuels.

58 Tian et al. [16] derived a semi-empirical correlation for the penetration distance of high-
59 pressure gasoline sprays based on their experimental study of p-xylene sprays in a CVC at non-
60 evaporating conditions (300 K) and evaporating conditions (500-760 K). Tian et al. [16]
61 compared spray penetration data at injection pressures between 200 and 1200 bar at a chamber

62 pressure of one bar (for non-evaporative conditions) and 10 to 40 bar (for evaporative
63 conditions). The correlation for penetration distance as a function of time used parameters found
64 in previous diesel spray correlations, including the difference between the fuel injection pressure
65 and the chamber pressure, nozzle outlet diameter, fuel density, and ambient density, and the
66 authors included ambient temperature as a means to include vaporization effects. Importantly,
67 the correlation by Tian et al. [16] did not propose a spray break-up time, which has been widely
68 used for diesel spray correlations. The correlation was compared with experimental results for
69 high-pressure gasoline sprays in the study by Medina et al. [17]. The comparisons showed
70 significant discrepancies at all times, which may be due to the lack of a transition in spray
71 development, i.e., omission of a spray break-up time in their model.

72 The recent study by Yamaguchi et al. [18] included spray studies using n-heptane and
73 various nozzle geometries at pressures up to 1500 bar. The authors found divergent nozzles
74 produced shorter penetration than convergent nozzles. Using droplet size measurements, they
75 also concluded increased injection pressure yields smaller droplets with the most pronounced
76 decrease at injection pressures of 800 bar. Given the study was conducted using n-heptane, it
77 would be valuable to confirm if the trends observed are consistent for multi-component gasoline.

78 In addition to fuel effects, experimental data for high-pressure gasoline sprays at broader
79 operating conditions are needed to guide engine development, to advance spray theory, and to
80 resolve discrepancies in existing data. Based on this need, the objective of the current study was
81 to systematically quantify high-pressure gasoline fuel spray development including the effects of
82 different internal nozzle geometries with a range of high-fidelity diagnostics.




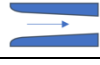
83

84 **Experimental Methodology**

85 In this study, two multi-hole prototype research grade fuel injectors were studied in three
86 experimental facilities. The key features of the internal geometry of each orifice are provided in
87 Table 1. Further details are discussed in Medina et al. [19]. Two experimental facilities were
88 used to measure the time-resolved mass flow rate and the time resolved momentum of the sprays.
89 A high-temperature and high-pressure facility was used to visualize the external spray
90 development using high-speed schlieren imaging. The fuel properties of the gasoline used in the
91 study are listed in Table A1 of the Appendix. For each of the measurements, the fuel was
92 pressurized using a custom piston pump and supplied to the injector through a common rail

93 system. Injection events were electronically controlled using an impulse generator (Genotec).
 94 The energize time for all injection events was set to 1 ms, similar to the experiments conducted
 95 in Medina et al. [17,19], to simulate typical gasoline direct injection performance and to
 96 represent transient injector behavior.

97 Table 1. Injector nozzle characteristics

Injector	Orifice No.	Normalized outlet diameter*	Conicity of nozzle passage**	Hydro-erosion rounding of nozzle inlet	Schematic of nozzle cross-section
X	Hole 1	0.578	0	0%	
	Hole 2	1	0	0%	
Y	Hole 1	0.789	-1.5	20%	
	Hole 2	0.789	3.5	20%	

98 * Hole diameter was normalized to the largest hole diameter

99 ** Nozzle conicity was measured relative to the nozzle exit diameter, where a straight nozzle had a conicity of 0, a
 100 converging nozzle had a positive conicity, and a diverging nozzle had a negative conicity.

101 102 *Instantaneous Mass Flow Rate Characterization*

103 A commercially available injection rate discharge curve indicator (IRDCI) (IAV, type N-
 104 050-028), which employs the Bosch method [20], was used to measure the instantaneous mass
 105 flow rate of the sprays from the injectors, i.e., the rate of injection (ROI). The IRDCI consists of
 106 a pressure transducer, a long fuel-filled tube, a large fuel reservoir, a relief valve, and a back-
 107 pressure cavity typically filled with nitrogen to reduce pressure oscillations. A schematic of the
 108 IRDCI is shown in Figure A1 of the Appendix. Details on the fundamental working principle are
 109 provided in previous studies [20–22]. The functionality of the facility is briefly described here.
 110 Fuel is injected into the long fuel-filled tube at the start of the test. The fuel injection event
 111 produces a pressure wave that is proportional to the instantaneous mass flow rate. The pressure
 112 wave is detected using a fast-response piezoelectric pressure sensor. The underlying theory is
 113 based on the hydraulic pulse theorem [20–22]. To account for uncertainties in the measurement
 114 related to the speed of sound, fuel is collected at the outlet of the IRDCI at the same rate at which
 115 fuel is being added to the reservoir. The fuel is collected on a mass balance, serving as a second
 116 mass flow rate measurement and for comparison with the IRDCI pressure-based measurements.
 117 The experimental error associated with the IRDCI measurements of fuel mass flow rate is less
 118 than 0.6% [22,23].

119 For each IRDCI experiment, the injector is placed in a cooling jacket that is fixed at the
 120 entrance of the IRDCI. The cooling jacket provides a continuous flow of temperature-controlled
 121 coolant, and thus the injector temperature is considered the same as the coolant temperature. Four
 122 injection pressures, three chamber pressures, and two coolant temperatures were tested and are
 123 listed in Table 2. Two sets of data with 50 repetitions each were collected at each condition. The
 124 first data set was used to verify stability and repeatability, and the second data set was used for
 125 analysis.

126 Table 2. Summary of experimental conditions

Parameter	Facility		
	IRDCI	Momentum Flux	CPF Reactor
Chamber gas	-	Nitrogen	Nitrogen
Fuel type	Reference gasoline		
Injector Tested	X and Y (see Table 1)		
Injection Pressures [bar]	600, 900, 1200, 1500		
Chamber Pressure [bar]	10, 20, 30	5, 10, 20, 30	5, 10, 20, 30
Chamber Temperature [K]	293	293	400, 600, 800
Coolant Temperature [K]	293, 363	363	293, 363
Number of repetitions	100	100	20

127

128 *Instantaneous Momentum Characterization*

129 The momentum rate meter is a custom-designed enclosed vessel with high-pressure
 130 chamber capabilities and optical access. The underlying assumptions and details of the system
 131 are presented in previous studies [24]. A schematic of the spray momentum rate meter is
 132 provided in Figure A2 of the Appendix. A brief summary of the operation is provided here. For a
 133 typical experiment, the chamber is pressurized with nitrogen to conditions consistent with the
 134 injection timing in a piston engine of interest. Momentum measurements are acquired using a
 135 piezoelectric sensor aligned perpendicular to the axis of the fuel spray. Only one spray plume is
 136 allowed to impact the sensor in the tests. The impact force of the spray plume is directly related
 137 to the axial momentum flux of the spray.

138 For the current work, the sensor target area was placed 8 mm from the nozzle outlet. This
 139 was the minimum distance to ensure no interference between the two plumes. This small
 140 distance also avoids potential losses from the spray due to atomization and evaporation. Similar
 141 to the IRDCI tests, two data sets of 50 measurements each were recorded. Four fuel injection

142 pressures, four chamber pressures, and one coolant temperature were tested. The complete list of
143 conditions is provided in Table 2.

144

145 *High-speed imaging characterization*

146 A custom-designed, high-temperature, high-pressure test facility was used to image the
147 gasoline spray development. A detailed description of the facility is presented in Payri et al. [25].
148 A brief summary of the facility and the experimental approach is provided here. The facility is a
149 constant-pressure flow (CPF) reactor with the ability to create nearly quiescent and steady
150 thermodynamic conditions [26]. During an experiment, the chamber is continuously pressurized
151 with nitrogen to simulate engine conditions and has three orthogonal optical access ports each
152 with viewing access of 12.8 cm. The chamber is rated to a maximum temperature of 1000 K and
153 a maximum pressure of 150 bar. A schematic of the CPF reactor is provided in Figure A3 of the
154 Appendix. The operating conditions used in the reactor experiments are listed in Table 2.

155 Schlieren imaging has been used extensively to visualize spray development [10,27–29].
156 The imaging technique used in this study was a single pass schlieren setup. A schematic of the
157 optical arrangement is shown Figure A4 of the Appendix. The technique consists of a light
158 source, collimating mirror, focusing lens, diaphragm, and camera. The light from a mercury-
159 xenon arc lamp is passed through a pin-hole with a diameter of 1.2 mm. The light is reflected
160 from a 150 mm parabolic mirror with a focal length of 650 mm, collimating the light through the
161 test section. After passing through the test section, the light is focused with a 150 mm biconvex
162 lens onto a diaphragm placed at the focal point of 450 mm. The diaphragm is set to a diameter of
163 4 mm and in front of the high-speed camera (Photron Fastcam SA5). The images were recorded
164 using a 100 mm lens (Zeiss) with the camera and the camera settings are listed in Table A2 of
165 the Appendix.

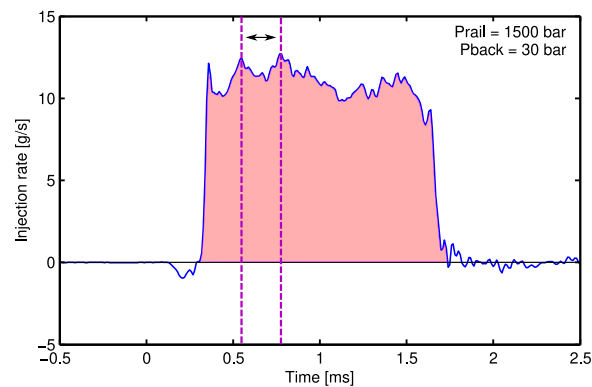
166

167 *Data Processing*

168 The data collected in the three facilities were processed using methods specific to each
169 experimental approach. Details are provided in references [23,24,28,30], and the approaches are
170 briefly summarized here.

171 The IRDCI data from all 50 injection events were averaged and converted to mass flow
172 rates/ROI, including corrections for signal bias, using the methods described in Bosch et al. [20],

173 and Payri et al. [23]. The ROI data were then integrated to obtain the total injected mass. The
 174 calculated mass was compared with the measurement from the mass balance. Using both
 175 measurements, a scaling factor was determined and used to correct the IRDCI measurements. An
 176 example of the corrected ROI signal is shown in Figure 1 along with the integrated mass,
 177 indicated by the shaded area. For each time-history of mass flow rate, a region was selected for
 178 analysis after the start of injection and before the end of injection, where the injection rate was
 179 relatively stable as a function of time and consistent across all injection events. For this study,
 180 the region used for the calculation for all injection events was characterized by the two peaks
 181 shown with dashed lines in Figure 1. The ROI data in this region were mathematically averaged
 182 and identified as the characteristic injection rate for each experiment. The ROI data were then
 183 used to calculate hydraulic coefficients such as the momentum coefficient and discharge
 184 coefficient for each injector. Variability in the time interval selected for analysis was considered
 185 in the uncertainty of the hydraulic coefficients determined from the data.
 186



187
 188 Figure 1. Rate of injection (ROI) results for 1500 bar injection pressure and 30 bar back pressure for Injector Y. The data include
 189 the mass from both nozzle holes of the injector. The shading represents the total mass per injection event. The vertical dashed
 190 lines indicate the region of the ROI data used as the characteristic injection rate.
 191
 192

193 The characteristic momentum flux values were determined using similar methods as used
 194 to determine the characteristic ROI. A time region with consistent behavior was used to
 195 determine the average momentum flux for each operating condition. Figure 2 shows an example
 196 of the momentum flux measurement where the stabilized range is indicated with vertical dashed
 197 lines. The uncertainty in the characteristic momentum flux values reported here is $\pm 2\%$ and is
 198 primarily due to the variability in the time interval selected.

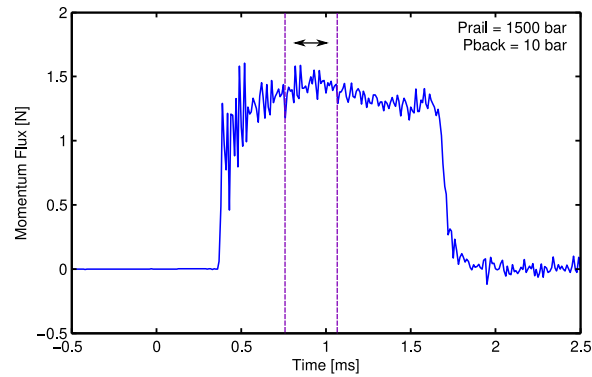
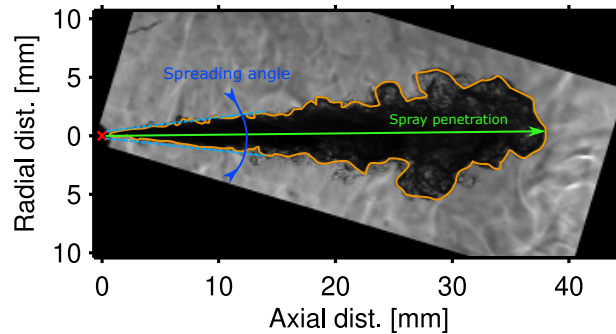


Figure 2. Momentum flux measurement for 1500 bar injection pressure and 10 bar chamber pressure. The vertical dashed lines indicate the stabilized region used to determine the average momentum flux for the operating condition.

199
200
201
202
203
204
205
206
207
208
209
210
211
212
213
214
215
216
217
218
219
220
221

The high-speed schlieren images were used to quantify the spray development in terms of spray tip penetration and spray angle. The image processing included four major steps: image masking, background subtraction, contour detection, and contour analysis. Figures showing intermediate results of the image analysis are provided in the Appendix (Figures A5). Image masking was determined by defining the general area where the sprays were located using the centerline axis of the sprays and the maximum anticipated width of the spray, creating a segmented triangular shape. To perform accurate background subtraction, two algorithms were implemented: dynamic background subtraction and image temporal derivative. The algorithms are complementary because the dynamic background captures a majority of the dense regions of the spray and the image temporal derivative captures the dilute fluid regions. Once each spray was isolated, contour detection was performed using binary images. Spray tip penetration distance and spray angle were calculated for each time step using the contours from the binary images. A typical processed image is shown in Figure 3 along with examples of measurements of penetration distance and spray angle (defined as the angle at one-third the penetration distance of the spray). Additional details on the image processing algorithms can be found in the literature [6,28,29]. The uncertainty in the penetration distance and the spray angle was 0.5% and 1.5%, respectively, and is primarily due to the parameters used in the image processing, e.g., the threshold applied to create the binary images.



222

223

224

Figure 3. Typical processed image of spray with plume contour shown in orange, spray tip penetration shown in green, and spray angle shown in blue.

225 Results

226

227

228

229

230

231

232

Mass Flow Rate

233

234

235

236

237

238

239

240

241

242

243

244

245

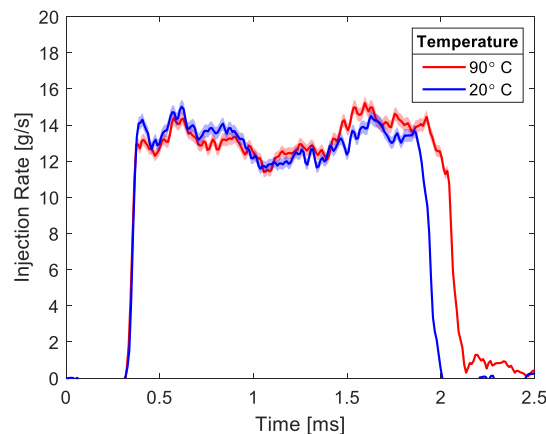
246

247

Figure 4 shows the injection rate results for two coolant temperatures (20 °C and 90 °C) for Injector Y at 1500 bar injection pressure and 20 bar chamber pressure. The averages are shown as solid lines and the standard deviations of 50 repetitions are shown as the shaded regions. All the injection events show the coolant temperature of 90° C resulted in a slightly longer injection event than the lower temperature conditions. The other portions of the injection event were very similar, with similar opening profiles and similar overall behavior for much of the event. Two methods were used to determine the mass difference between the injection events at different coolant temperatures. The first considers the additional time of injection multiplied by the average or representative injection rate. In Figure 4 the higher coolant temperature resulted in a ~120 μ s longer injection event, corresponding to about ~1.5 mg more fuel injected compared with the lower temperature condition. The second method is a mathematical integration of the injection rate data. The mathematical integration showed a difference of ~2 mg or 9% between the coolant temperatures. The difference between the values is due to small differences in the injection rate profiles at the different coolant temperatures. The integrated mass for a majority of the conditions tested showed the higher coolant temperature yielded

248 between 1% and 5% more fuel primarily due to longer injection events. For clarity and emphasis,
 249 Figure 4 shows the case with the highest difference in integrated mass. Other examples are
 250 provided in the Appendix.

251 One explanation for the trend of more mass injected at higher fuel injector temperatures
 252 may be related to fuel viscosity. Higher temperatures result in lower viscosity, thus reducing the
 253 viscous forces required to close the needle at the end of injection. Salvador et al. [21] noticed the
 254 same behavior with diesel fuel for multiple injection durations and injection pressures using a
 255 solenoid injector. Salvador et al. [21] concluded that higher viscous forces at lower temperatures
 256 reduce the maximum needle lift, such that the needle closes from a lower position at lower
 257 temperatures. This reduces the time needed to close the injector. Guangxin et al. [31] reported
 258 similar behavior with dimethyl ether and increasing fuel temperature, attributing the extended
 259 injection duration at higher temperatures to changes in fuel properties. Another factor that may
 260 affect injection rate is the mechanical operation of the solenoid actuator similar to the
 261 temperature effects on piezoelectric driven injectors [32–34]. Both fuel properties and
 262 mechanical operation may impact the injection duration.



263
 264 Figure 4. Average fuel injection rate for two coolant temperatures for Injector Y Holes 1 and 2 at 1500 bar injection pressure and
 265 20 bar chamber pressure
 266
 267

268 The effects of chamber pressure on injection rate were also investigated. The results show
 269 the injection rate was similar for the three chamber pressures of 10, 20, and 30 bar with
 270 significant differences only occurring during the injector opening events. See Figure A7 of the
 271 Appendix for typical results. Lower chamber pressure exhibited a spike in injection rate during
 272 the opening event (with overshoots of a factor of 1.2 to 1.4), particularly at higher injection
 273 pressures. This behavior may be due to the limit of the dynamic response of the IRDCI; the

274 lowest rated pressure for the equipment is 10 bar suggesting higher uncertainty and noise in the
 275 measurement at lower chamber pressures. Excluding the variation at the start of injection, the
 276 results show chamber pressure has minor to negligible effects on injector rate, which is
 277 consistent with previous studies of other fuels and injectors [20,35].

278 The effects of injection pressure on injection rate were consistent with expectations based
 279 on previous studies in the literature. Typical results are presented in the Appendix in Figure A8.
 280 Increasing fuel injection pressure increased the fuel mass flow rate for the same injection timing
 281 due to higher flow velocities. In addition, higher injection pressures resulted in slightly earlier
 282 end of injection. This trend was consistent across chamber pressures and the injectors tested at
 283 lower coolant temperatures. However, when the coolant temperature was increased to 90° C, the
 284 needle opening and closing events were almost identical for most conditions. This trend may be
 285 attributable to the fuel viscosity or mechanical operation of the solenoid actuator as discussed
 286 earlier. However, there was one exception for the data at higher coolant temperatures for Injector
 287 Y at an injection pressure of 600 bar. At these conditions, the mass flow rate data indicate later
 288 needle closing.

289 The hydraulic parameters for each nozzle were determined from the mass flow rate and
 290 momentum flux measurements. The characteristic value for each measurement was used for the
 291 analysis to determine the momentum coefficient, discharge coefficient, effective area, and
 292 effective outlet velocity. The discharge coefficient, C_d , was calculated according to Equation 1
 293 using the measured, \dot{m} , and the theoretical, \dot{m}_t , mass flow rates. All the coefficients were derived
 294 from first principles, and additional details and assumptions are provided in the references [24].

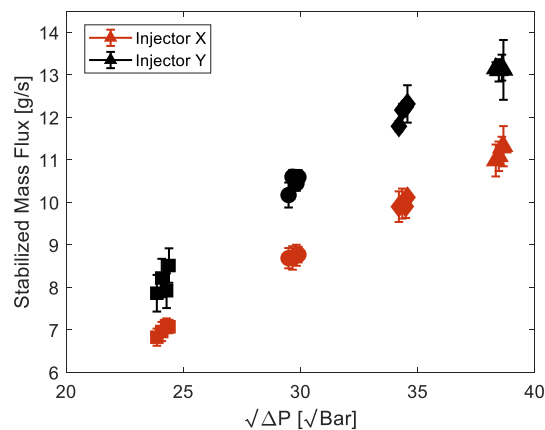
$$295 \quad C_d = \frac{A_{eff} \rho_f U_{eff}}{A_o \rho_f U_t} = \frac{\dot{m}}{\dot{m}_t} = \frac{\dot{m}}{A_o \sqrt{2 \rho_f \Delta P}} \quad (1)$$

296 Where A_o is the outlet area, A_{eff} is the effective area, U_{eff} is the effective velocity, U_t is the
 297 theoretical velocity, ρ_f is density of the fluid, and ΔP is the difference between fuel injection
 298 pressure and chamber pressure.

299 Figures 5 presents the ROI results for both injectors tested at 90° C for all injection and
 300 chamber pressures as a function of $(\Delta P)^{1/2}$. The data show, as expected based on Bernoulli's
 301 approximation for flow velocity (Equation 1), that ROI is linearly proportional to $(\Delta P)^{1/2}$ and that
 302 Injector Y consistently produced a higher mass flow rate compared with Injector X. The
 303 differences between Injector X and Injector Y are the conicity, inlet hole rounding of the nozzles

304 and nozzle diameters. Injector X has two cylindrical nozzles, one with a slightly larger diameter
 305 and one with a slightly smaller diameter than the nozzles of Injector Y. The total physical nozzle
 306 outlet diameter (and therefore total nozzle outlet area) for each injector is the same. So the trends
 307 may be attributed to the effects of rounding the nozzle inlet (Injector Y) and uniform (Injector X)
 308 versus converging/diverging nozzle channel (Injector Y). The mass flow rates for Injector X
 309 were consistently lower than the mass flow rates of Injector Y, by 11% to 22%, with the smallest
 310 difference observed at injection pressures of 600 bar and the highest difference observed at
 311 injection pressures of 1200 bar. Assuming the conicity effects for both orifices of Injector Y are
 312 offsetting, the results indicate rounding has a measurable impact on mass flow rate. Recall,
 313 hydro-erosion increases the static flow rate by rounding the nozzle inlet edges. Although the
 314 increase in mass flow rate is less than the increase in static flow rate, the percentage of hydro-
 315 erosion rounding is consistent with the percent increase in the static flow rate.

316 The discharge coefficient as a function of Reynolds number for both injectors tested at
 317 90° C for all injection and chamber pressures is shown in Figure 6. Injector Y has consistently
 318 higher discharge coefficients, by 24% to 37%, compared with Injector X for all tested conditions.
 319 The increased discharge coefficient is attributed to the rounded nozzle inlet edges in Injector Y.
 320 Injector X shows a relatively constant discharge coefficient at all Reynolds numbers, which
 321 could be an indication of cavitation [24,36–38]; however, Injector Y is also likely cavitating
 322 (discussed further below) and shows some sensitivity of the discharge coefficient to Reynolds
 323 number. Thus, there are likely additional factors affecting C_d for the injectors.



324 Figure 5. Characteristic mass flux results for 90° C coolant temperature. The error bars represent the variability in the time
 325 interval selected for the characteristic value.
 326

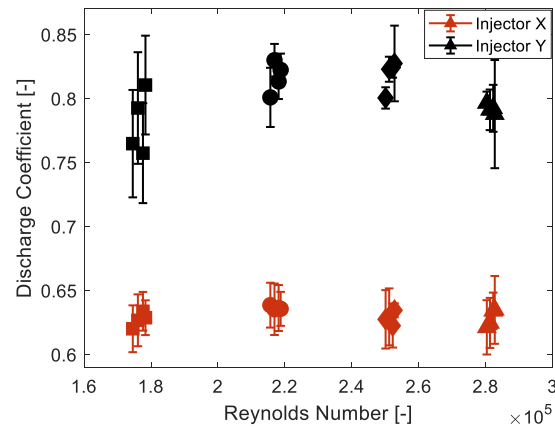


Figure 6. Discharge coefficient results for 90° C coolant temperature. The error bars represent the variability in the time interval selected for the characteristic value.

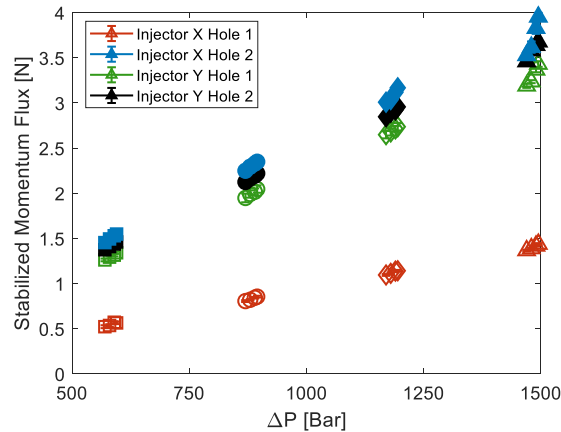
327
328
329

330 *Momentum Flux*

331 The results for momentum flux for chamber pressures of 5 to 30 bar were virtually
332 identical for all chamber pressures, which is consistent with expectations based on the theory and
333 principles used to design the facility [24]. Briefly, as long as the sensor is placed a reasonable
334 distance from the orifice and orthogonal to the spray, the momentum of the jet is unaffected by
335 the chamber density. Increasing injection pressure resulted in an increase in momentum flux, and
336 higher variability in the momentum measurement was observed for higher chamber pressures for
337 all injection pressures. Typical momentum flux time-history data are provided in the Appendix
338 for reference (Figures A9 and A10).

339 Figure 7 presents the results for the characteristic momentum flux measurements as a
340 function of ΔP , and, like the mass flow rate measurements, the results show linear dependence.
341 Here the momentum flux data are resolved to the level of the individual nozzles of the injectors.
342 Injector X Hole 2, with the largest outlet diameter, resulted in the highest momentum flux at all
343 test conditions. At the opposite end of the spectrum, Injector X Hole 1, with the smallest outlet
344 diameter, resulted in the smallest momentum flux at all test conditions. The intermediate results
345 for Injector Y Holes 1 and 2, were close to the values for the largest nozzle diameter, Injector X
346 Hole 2. On average the difference between the nozzles with the highest momentum flux, Injector
347 X Hole 2 and Injector Y Hole 2, is 6%. Between Injector Y Holes 1 and 2, the differences ranged
348 between 7 to 9% for all conditions. Injector Y Holes 1 and 2 have the same outlet diameter but,
349 differ in conicity. Injector Y Hole 2 has a converging nozzle resulting in higher outlet velocities
350 compared with Injector Y Hole 1, which is reflected in the momentum flux data. Overall, the

351 trends indicate the size of the nozzle outlet diameter has a stronger effect on momentum flux
 352 than conicity or hydro-erosion rounding.



353 Figure 7. Characteristic momentum flux results for 90° C coolant temperature. The error bars are smaller than the symbols and
 354 they represent the variability in the time interval selected for the characteristic value.
 355
 356

357 The theoretical momentum flux can be calculated using ΔP and the Bernoulli principle
 358 for comparison with the experimental data. The ratio between the measured momentum flux, \dot{M} ,
 359 and theoretical momentum flux, \dot{M}_t , can then be calculated to obtain the momentum coefficient,
 360 C_M , for each nozzle similar:

$$361 \quad C_M = \frac{A_{eff} \rho U_{eff}^2}{A_o \rho U_t^2} = \frac{\dot{M}}{\dot{M}_t} = \frac{\dot{M}}{2A_o \Delta P} \quad (2)$$

362 The momentum coefficient results are shown in Figure 8 for the four orifices. Two trends
 363 are observed. The first is the relative performance of the different injector geometries. The
 364 nozzles with hydro-erosion rounding (Injector Y) yielded systematically higher momentum
 365 coefficients. Hydro-erosion rounding is used to reduce the amount of flow separation and
 366 increase the effective area, and the results show rounding does improve nozzle performance,
 367 more closely approximating the theoretical value. Injector Y Holes 1 and 2 have the same outlet
 368 diameters, but with diverging and converging nozzle passages, respectively. The data show the
 369 larger inlet diameter associated with the converging nozzle of Injector Y Hole 2 further reduces
 370 flow separation compared with the diverging nozzle. The uniform cross-section/cylindrical
 371 nozzles both exhibited lower momentum coefficients, which is attributed to increased flow
 372 separation or reduced effective area.

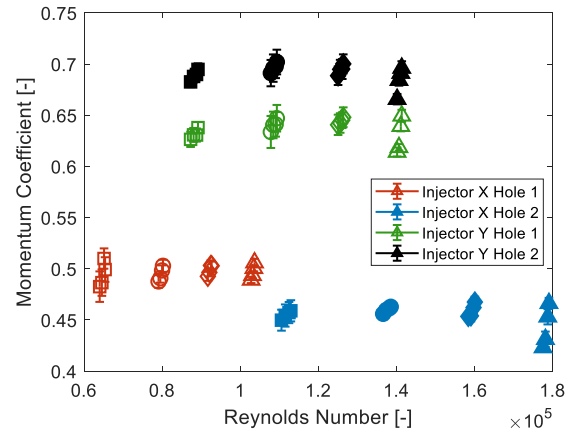


Figure 8. Momentum coefficient results for 90° C coolant temperature. The error bars represent the variability in the time interval selected for the characteristic value.

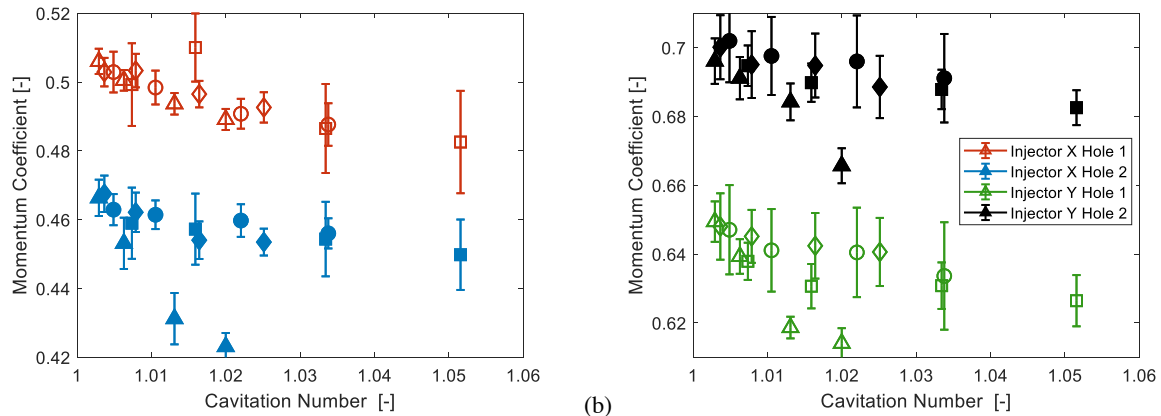
373
374
375
376

377 The data also show the momentum coefficient is independent of Reynolds number. Under
378 cavitating conditions, the discharge coefficient only depends on the cavitation number and not on
379 Reynolds number [24,36,37], as shown in Equation 3:

$$380 \quad C_d = C_c \sqrt{K} = \frac{C_M}{C_v} \quad (3)$$

381 Although some of the nozzle geometries included features to reduce the probability of cavitation,
382 such as the hydro-erosion rounding of the nozzle inlet, all nozzles exhibited this behavior at 90°
383 C coolant temperature. The fuel properties of gasoline combined with the trends observed with
384 the momentum coefficient as a function of high Reynolds number support the conclusion that the
385 nozzle flows experience cavitation.

386 Figure 9 shows the momentum coefficient as a function of cavitation number for the four
387 orifices, where the cavitation number is defined based on the study by Nurick [37]. All four
388 orifices show a decreasing trend in momentum coefficient with increasing cavitation number.
389 Several studies have suggested that once cavitation starts, the discharge coefficient is only
390 dependent on cavitation number and essentially independent of Reynolds number [24,37,39,40].
391 The same studies state that large cavitation numbers suggest non-cavitating flow while small
392 cavitation numbers (close to 1) correspond to strong cavitating flow. The prior discussions are
393 with respect to the discharge coefficient, and Figure 9 shows the momentum coefficient.
394 However, the discharge coefficient and the momentum coefficient are linearly dependent, as
395 shown in Equation 3, suggesting that under cavitating conditions, the momentum coefficient is a
396 function of the cavitation number.



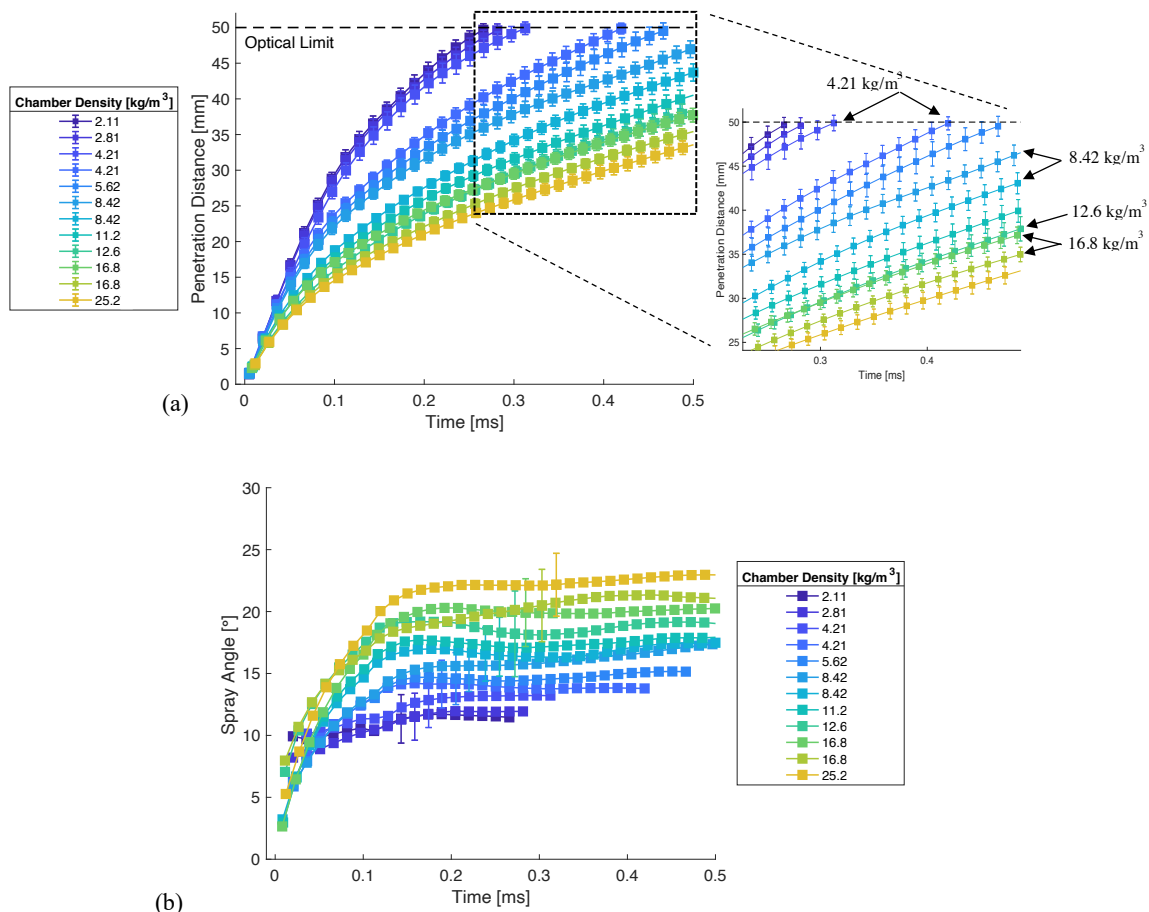
397
398
399
(a) Figure 9. Momentum coefficient results for the four orifices of (a) Injector X and (b) Injector Y for 90° C coolant temperature. The error bars represent the variability in the time interval selected for the characteristic value.

400 External spray features such as spray flutter observed and discussed in Medina et al. [19]
401 using the same injectors support the conclusion that the flow was cavitating. Spray flutter was
402 suspected to be a product of surface roughness, machining defects and/or cavitation. Cavitation
403 was considered more likely due to the fuel volatility and the operating conditions. Thus, several
404 observations indicate the flow is cavitating at all operating conditions for all orifices. To
405 summarize, the downstream external spray features such as spray flutter [19], the cavitation
406 numbers close to 1, the fuel properties, and the negative trend of momentum coefficient with
407 increasing cavitation number all suggest that the nozzles are experiencing cavitation. This is an
408 important conclusion that should be considered when interpreting the other spray measurements
409 and when considering injector design for high-pressure gasoline sprays.

410 411 *Visual Spray Development*

412 Several chamber temperatures and pressures were tested resulting in 12 total
413 combinations and nine unique chamber densities from 2.11 to 25.27 kg/m³. Three chamber
414 densities were repeated but, using a combination of different chamber conditions. Figure 10
415 shows the average penetration distance for Injector X Hole 1 at 1500 bar injection pressure and
416 90° C coolant temperature for the 12 chamber conditions. Since the results are based on schlieren
417 imaging, the data include the vapor- and liquid-phase regions of the fuel spray. The data in
418 Figure 10 are averages of 20 repetitions with error bars representing one standard deviation. In
419 the figure, the data are clustered in three groupings with similar penetration behavior. The
420 groupings are due to the different chamber pressures. The fastest penetration data are from the
421 experiments with 5 bar chamber pressure. The slowest penetration data are from the highest

422 chamber pressures of 20 and 30 bar. The smaller differences in the penetration distances within
 423 each group are due to the different chamber temperatures. Amongst the same chamber pressure
 424 group, the highest temperature results in the fastest penetration due to the lower chamber density.
 425 Interestingly, the penetration and spray angle data from the three identical pairs of densities
 426 differ (4.21, 8.42 and 16.9 kg/m³), as seen in Figure 10. The trend shows the chamber pressure
 427 has a stronger effect on spray penetration distance than chamber temperature, particularly for
 428 lower chamber pressures. Also interesting is that for portions of the penetration distance time
 429 histories the data for 12.6 and 16.9 kg/m³ were identical, as seen in the inset of Figure 10. All
 430 these trends, with respect to the chamber density, chamber pressure and temperature, and the
 431 similar penetration data for 12.6 and 16.9 kg/m³, were observed to some degree for all nozzles
 432 and all injection pressures.



433

434

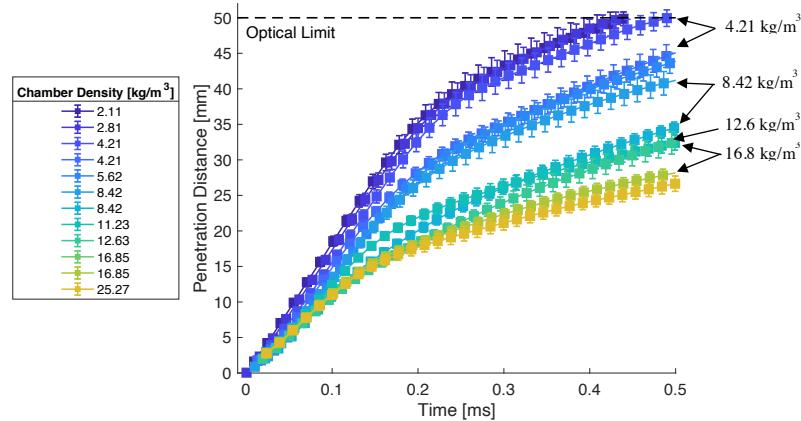
435 Figure 10. (a) Average penetration distance and (b) average spray angle for Injector X Hole 1 at 1500 bar injection pressure and
 436 90° C coolant temperature. The error bars are the standard deviation of 20 measurements.

437

438 At lower injection pressures, the groupings of data were more pronounced, with greater

439 division between the penetration distances, as seen in Figure 11 for Injector Y Hole 1 at 600 bar

440 injection pressure. The effects of temperature were smaller at lower chamber pressures, with
 441 more overlapping data. However, small differences were still observed between identical
 442 chamber densities.

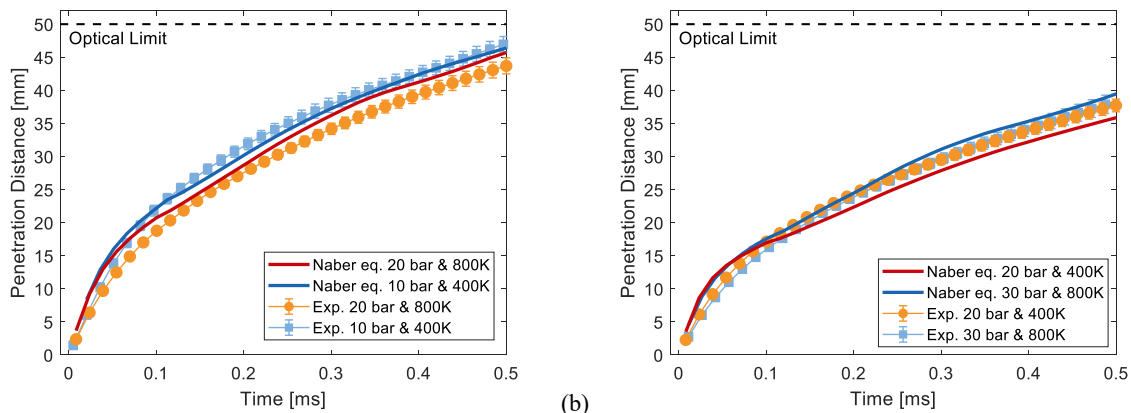


443 Figure 11. Average penetration distance for Injector Y Hole 1 at 600 bar injection pressure and 90° C coolant temperature. The
 444 error bars are the standard deviation of 20 measurements.
 445
 446

447 The grouping of the results observed in Figure 10 and 11 could be a product of the fuel
 448 properties that were studied. For example, Payri et al. [5] studied the spray characteristics of n-
 449 dodecane and n-heptane in a constant pressure flow reactor and reported that for the same
 450 chamber density, a change of 200 K in chamber temperature did not result in any difference in
 451 the penetration distance data. However, Naber and Siebers [3] studied diesel spray characteristics
 452 in a constant volume chamber at various chamber conditions and reported that for the same
 453 chamber density, increasing chamber temperature resulted in reduced penetration distance. The
 454 diesel spray characteristics of penetration distance for the same density are similar to the trends
 455 observed in this work with gasoline. Both diesel and gasoline are multicomponent fuels while the
 456 fuels studied in Payri et al. [5] were single component fuels. Comparing the results of the
 457 different studies indicates fuel composition and associated thermophysical properties affect the
 458 spray characteristics sufficiently to visibly impact spray penetration.

459 Several correlations have been previously developed for diesel and gasoline fuel sprays.
 460 Of the correlations developed for high fuel injection pressures, the work by Naber and Siebers
 461 [3] was selected for comparison here. As noted earlier, the correlation by Tian et al. [13] for high
 462 pressure gasoline sprays does not include two phases of spray development and did not agree
 463 well with the previous study of high-pressure gasoline sprays by Medina et al. [17]. Naber and
 464 Siebers derived a correlation for penetration distance as a function of time based on first

465 principles and the properties of diesel fuel sprays. The correlation is compared with the
 466 experimental data from the current work in Figure 12. In the figure, one panel compares data at
 467 the same chamber density, but with different chamber temperatures and pressures, and the other
 468 panel compares results from two different chamber densities. The difference between the
 469 predictions for the same density is less than 1 mm at each time step, and the difference between
 470 the experimental data sets for the same density is less than 4 mm. The diesel correlation predicts
 471 very similar penetration curves for the same density while the data shows some differences. The
 472 inverse is true for Figure 12b, where both experimental data are different densities but identical
 473 penetration curves. The diesel correlation shows a difference of at least 3mm. In spite of the
 474 differences, both panels show very good agreement between the experimental data and the diesel
 475 spray correlation for the entire time intervals (within ~8% throughout the time histories).
 476



477 (a)
 478 (b)
 479 Figure 12. Comparison of experimental results for Injector X Hole 1 with the spray correlation by Naber and Siebers [3] for (a)
 480 chamber density of 8.42 kg/m^3 and injection pressure of 1500 bar and (b) chamber density of 12.6 kg/m^3 and 16.8 kg/m^3 .

481 Conclusions

482 Three methods were used to measure mass flow rate, momentum flux and spray
 483 development of high-pressure gasoline fuel sprays using different internal nozzle geometries at a
 484 broad range of operating and experimental conditions. The major conclusions based on the
 485 results of the study are:

- 486 • Internal injector geometry played a considerable role on internal flow dynamics and
 487 hydraulic behavior. The mass injection data showed hydro-erosion rounding and conicity
 488 increased the mass flow rate between 11-22% compared with cylindrical/uniform cross-
 489 section nozzles. The momentum data showed larger nozzle diameters and converging and

- 490 rounded inlet nozzles could be used to achieve similar momentum fluxes, with
491 differences of between 5-7% in momentum flux between these two nozzle geometries.
- 492 • The combination of data showed all nozzles were cavitating, regardless of injector
493 temperature, nozzle geometry, chamber pressure and injection pressure, as determined by
494 the observed trends for momentum coefficient. Cavitation could be a cause of component
495 damage and can affect fuel flow rates, mixing and atomization.
 - 496 • Injector temperature had a noticeable effect on the injection rate. Temperature is
497 suspected to affect fuel viscosity impacting needle opening and closing events. For a
498 majority of the cases, higher coolant temperature led to 1% to 5% more fuel injected per
499 event.
 - 500 • In agreement with previous spray visualization studies, chamber pressure had a strong
501 effect on spray penetration, more so than chamber temperature, and the combined
502 parameter of chamber density.
 - 503 • While nozzle geometry had no effect on the early portion of the spray development,
504 nozzle geometry significantly influenced spray development at later times (e.g., after the
505 spray break-up time), producing similar trends as those observed with the momentum
506 flux measurements.

507

508 **Acknowledgements**

509 The authors would like to acknowledge the generous support of the Mechanical
510 Engineering Department and the Rackham Graduate School at the University of Michigan. The
511 work was also made possible through collaboration with the Engine Research Division, Centro
512 Motores Termicos at Universitat Politecnica de Valencia. We would like to offer special thanks
513 to the faculty, technicians and graduate students at Universitat Politecnica de Valencia that
514 contributed their time and expertise to the work.

515

516 **Reference**

- 517 [1] Dec JE. A Conceptual Model of DI Diesel Combustion Based on Laser-Sheet Imaging*.
518 SAE Tech. Pap., 1997. <https://doi.org/10.4271/970873>.
- 519 [2] Hiroyasu H, Arai M. Structure of Fuel Sprays in Diesel Engines. SAE Tech Pap 1990.
520 <https://doi.org/10.4271/900475>.

- 521 [3] Naber J, Siebers DL. Effects of Gas Density and Vaporization on Penetration and
522 Dispersion of Diesel Sprays. SAE Tech Pap 1996. <https://doi.org/10.4271/960034>.
- 523 [4] Taşkıran ÖO, Ergeneman M. Experimental Study on Diesel Spray Characteristics and
524 Autoignition Process. J Combust 2011;2011. <https://doi.org/10.1155/2011/528126>.
- 525 [5] Payri R, Viera JP, Gopalakrishnan V, Szymkowicz PG. The effect of nozzle geometry
526 over internal flow and spray formation for three different fuels. Fuel 2016;183.
527 <https://doi.org/10.1016/j.fuel.2016.06.041>.
- 528 [6] Payri R, Gimeno J, Bracho G, Vaquerizo D. Study of liquid and vapor phase behavior on
529 Diesel sprays for heavy duty engine nozzles. Appl Therm Eng 2016;107:365–78.
530 <https://doi.org/10.1016/j.applthermaleng.2016.06.159>.
- 531 [7] Yao C, Geng P, Yin Z, Hu J, Chen D, Ju Y. Impacts of nozzle geometry on spray
532 combustion of high pressure common rail injectors in a constant volume combustion
533 chamber. Fuel 2016;179:235–45. <https://doi.org/10.1016/j.fuel.2016.03.097>.
- 534 [8] Eagle EW, Morris SB, Wooldridge M. High-speed imaging of transient diesel spray
535 behavior during high pressure injection of a multi-hole fuel injector. Fuel 2014;116:299–
536 309. <https://doi.org/10.1016/j.fuel.2013.07.120>.
- 537 [9] Desantes JM, Payri R, Salvador FJ, De La Morena J. Influence of cavitation phenomenon
538 on primary break-up and spray behavior at stationary conditions. Fuel 2010;89:3033–41.
539 <https://doi.org/10.1016/j.fuel.2010.06.004>.
- 540 [10] Skeen SA, Manin J, Pickett LM. Simultaneous formaldehyde PLIF and high-speed
541 schlieren imaging for ignition visualization in high-pressure spray flames. Proc Combust
542 Inst 2015;35:3167–74. <https://doi.org/10.1016/j.proci.2014.06.040>.
- 543 [11] Cancino LR, da Silva A, De Toni AR, Fikri M, Oliveira AAM, Schulz C, et al. A six-
544 compound, high performance gasoline surrogate for internal combustion engines:
545 Experimental and numerical study of autoignition using high-pressure shock tubes. Fuel
546 2020;261. <https://doi.org/10.1016/j.fuel.2019.116439>.
- 547 [12] Xuan T, EL-Seesy AI, Mi Y, Lu P, Zhong W, He Z, et al. Effects of an injector cooling
548 jacket on combustion characteristics of compressed-ignition sprays with a gasoline-
549 hydrogenated catalytic biodiesel blend. Fuel 2020;276.
550 <https://doi.org/10.1016/j.fuel.2020.117947>.
- 551 [13] Du J, Mohan B, Sim J, Fang T, Roberts WL. Macroscopic non-reacting spray

- 552 characterization of gasoline compression ignition fuels in a constant volume chamber.
553 Fuel 2019;255:115818. <https://doi.org/10.1016/j.fuel.2019.115818>.
- 554 [14] Kim K, Kim D, Jung Y, Bae C. Spray and combustion characteristics of gasoline and
555 diesel in a direct injection compression ignition engine. Fuel 2013;109:616–26.
556 <https://doi.org/10.1016/j.fuel.2013.02.060>.
- 557 [15] Payri R, Garcia A, Domenech V, Durrett R, Plazas AH. An experimental study of gasoline
558 effects on injection rate, momentum flux and spray characteristics using a common rail
559 diesel injection system. Fuel 2012;97:390–9. <https://doi.org/10.1016/j.fuel.2011.11.065>.
- 560 [16] Tian J, Zhao M, Long W, Nishida K, Fujikawa T, Zhang W. Experimental study on spray
561 characteristics under ultra-high injection pressure for DISI engines. Fuel 2016;186:365–
562 74. <https://doi.org/10.1016/j.fuel.2016.08.086>.
- 563 [17] Medina M, Fatouraie M, Wooldridge M. High-Speed Imaging Studies of Gasoline Fuel
564 Sprays at Fuel Injection Pressures from 300 to 1500 bar. SAE Tech Pap 2018;c:1–18.
565 <https://doi.org/10.4271/2018-01-0294>.
- 566 [18] Yamaguchi A, Koopmans L, Helmantel A, Karrholm FP, Dahlander P. Spray
567 Characterization of Gasoline Direct Injection Sprays Under Fuel Injection Pressures up to
568 150 MPa with Different Nozzle Geometries. SAE Tech Pap Ser 2019;1:1–14.
569 <https://doi.org/10.4271/2019-01-0063>.
- 570 [19] Medina M, Zhou Y, Fatouraie M, Wooldridge M. High-Speed Imaging Study on the
571 Effects of Internal Geometry on High-Pressure Gasoline Sprays. SAE Tech. Pap., 2020.
572 <https://doi.org/10.4271/2020-01-2111>.
- 573 [20] Bosch W. The Fuel Rate Indicator: A New Measuring Instrument For Display of the
574 Characteristics of Individual Injection. SAE Tech Pap Ser 1968;1.
575 <https://doi.org/10.4271/660749>.
- 576 [21] Salvador FJ, Gimeno J, Carreres M, Crialesi-Esposito M. Fuel temperature influence on
577 the performance of a last generation common-rail diesel ballistic injector. Part I:
578 Experimental mass flow rate measurements and discussion. Energy Convers Manag
579 2016;114:364–75. <https://doi.org/10.1016/j.enconman.2016.02.042>.
- 580 [22] Payri R, Gimeno J, Martí-Aldaraví P, Viera A. Measurements of the mass allocation for
581 multiple injection strategies using the rate of injection and momentum flux signals. Int J
582 Engine Res 2020. <https://doi.org/10.1177/1468087419894854>.

- 583 [23] Payri R, Salvador FJ, Gimeno J, Bracho G. A new methodology for correcting the signal
584 cumulative phenomenon on injection rate measurements. *Exp Tech* 2008;32:46–9.
585 <https://doi.org/10.1111/j.1747-1567.2007.00188.x>.
- 586 [24] Payri R, García JM, Salvador FJ, Gimeno J. Using spray momentum flux measurements to
587 understand the influence of diesel nozzle geometry on spray characteristics. *Fuel*
588 2005;84:551–61. <https://doi.org/10.1016/j.fuel.2004.10.009>.
- 589 [25] Payri R, García-Oliver JM, Bardi M, Manin J. Fuel temperature influence on diesel sprays
590 in inert and reacting conditions. *Appl Therm Eng* 2012;35:185–95.
591 <https://doi.org/10.1016/j.applthermaleng.2011.10.027>.
- 592 [26] Meijer M, Somers B, Johnson J, Naber J, Lee SY, Malbec LM, et al. Engine Combustion
593 Network (ECN): Characterization and comparison of boundary conditions for different
594 combustion vessels. *At Sprays* 2012;22:777–806.
595 <https://doi.org/10.1615/AtomizSpr.2012006083>.
- 596 [27] Parrish SE. Evaluation of Liquid and Vapor Penetration of Sprays from a Multi-Hole
597 Gasoline Fuel Injector Operating Under Engine-Like Conditions. *SAE Tech Pap* 2014-04-
598 01 2014;7:1017–33. <https://doi.org/10.4271/2014-01-1409>.
- 599 [28] Pastor JV, Payri R, Garcia-oliver JM, Nerva J. Schlieren Measurements of the ECN-Spray
600 A Penetration under Inert and Reacting Conditions. *SAE Int* 2012.
601 <https://doi.org/10.4271/2012-01-0456>.
- 602 [29] Payri R, Salvador FJ, Bracho G, Viera A. Differences between single and double-pass
603 schlieren imaging on diesel vapor spray characteristics. *Appl Therm Eng* 2017;125:220–
604 31. <https://doi.org/10.1016/j.applthermaleng.2017.06.140>.
- 605 [30] Benajes J, Payri R, Molina S, Soare V. Investigation of the influence of injection rate
606 shaping on the spray characteristics in a diesel common rail system equipped with a piston
607 amplifier. *J Fluids Eng Trans ASME* 2005;127:1102–10.
608 <https://doi.org/10.1115/1.2062767>.
- 609 [31] Guangxin G, Zhulin Y, Apeng Z, Shenghua L, Yanju W. Effects of Fuel Temperature on
610 Injection Process and Combustion of Dimethyl Ether Engine. *J Energy Resour Technol*
611 2013;135:1–5. <https://doi.org/10.1115/1.4023549>.
- 612 [32] Payri R, Gimeno J, Mata C, Viera A. Rate of injection measurements of a direct-acting
613 piezoelectric injector for different operating temperatures. *Energy Convers Manag*

- 614 2017;154:387–93. <https://doi.org/10.1016/j.enconman.2017.11.029>.
- 615 [33] Mitrovic M, P. Carman G, K. Straub F. Response of piezoelectric stack actuators under
616 combined electro-mechanical loading. *Int J Solids Struct* 2001;38:4357–74.
617 [https://doi.org/10.1016/S0020-7683\(00\)00273-0](https://doi.org/10.1016/S0020-7683(00)00273-0).
- 618 [34] Ferrari A, Mittica A. FEM modeling of the piezoelectric driving system in the design of
619 direct-acting diesel injectors. *Appl Energy* 2012;99:471–83.
620 <https://doi.org/10.1016/j.apenergy.2012.05.048>.
- 621 [35] Payri R, Gimeno J, Marti-aldaravi P, Vaquerizo D. Internal Flow Characterization on an
622 ECN Injector. *At Sprays* 2015;26:889–919.
623 <https://doi.org/10.1615/atomizspr.2015013930>.
- 624 [36] Benajes J, Pastor JV, Payri R, Plazas AH. Analysis of the Influence of Diesel Nozzle
625 Geometry in the Injection Rate Characteristic. *J Fluids Eng* 2004;126:63.
626 <https://doi.org/10.1115/1.1637636>.
- 627 [37] Nurick WH. Orifice cavitation and its effect on spray mixing. *J Fluids Eng Trans ASME*
628 1977;99:426–7. <https://doi.org/10.1115/1.3448785>.
- 629 [38] Payri R, Gimeno J, Cuisano J, Arco J. Hydraulic characterization of diesel engine single-
630 hole injectors. *Fuel* 2016;180:357–66. <https://doi.org/10.1016/j.fuel.2016.03.083>.
- 631 [39] Sun Y, Guan Z, Hooman K. Cavitation in Diesel Fuel Injector Nozzles and its Influence
632 on Atomization and Spray. *Chem Eng Technol* 2019;42:6–29.
633 <https://doi.org/10.1002/ceat.201800323>.
- 634 [40] He Z, Guo G, Tao X, Zhong W, Leng X, Wang Q. Study of the effect of nozzle hole shape
635 on internal flow and spray characteristics. *Int Commun Heat Mass Transf* 2016;71:1–8.
636 <https://doi.org/10.1016/j.icheatmasstransfer.2015.12.002>.
- 637